Computer Methods and Programs in Biomedicine 147 (2017) 51–61

Contents lists available at ScienceDirect

Computer Methods and Programs in Biomedicine

journal homepage: www.elsevier.com/locate/cmpb

Joint optic disc and cup boundary extraction from monocular fundus images

Arunava Chakravarty*, Jayanthi Sivaswamy

Centre for Visual Information Technology, International Institute of Information Technology Hyderabad, 500032, India

ARTICLE INFO

Article history:
Received 4 February 2017
Revised 4 May 2017
Accepted 20 June 2017

Keywords:
Glaucoma
Optic disc
Optic cup
Depth reconstruction
Conditional Random Field
Coupled sparse dictionary

ABSTRACT

Background and objective: Accurate segmentation of optic disc and cup from monocular color fundus images plays a significant role in the screening and diagnosis of glaucoma. Though optic cup is characterized by the drop in depth from the disc boundary, most existing methods segment the two structures separately and rely only on color and vessel kink based cues due to the lack of explicit depth information in color fundus images.

Methods: We propose a novel boundary-based Conditional Random Field formulation that extracts both the optic disc and cup boundaries in a single optimization step. In addition to the color gradients, the proposed method explicitly models the depth which is estimated from the fundus image itself using a coupled, sparse dictionary trained on a set of image-depth map (derived from Optical Coherence Tomography) pairs.

Results: The estimated depth achieved a correlation coefficient of 0.80 with respect to the ground truth. The proposed segmentation method outperformed several state-of-the-art methods on five public datasets. The average dice coefficient was in the range of 0.87–0.97 for disc segmentation across three datasets and 0.83 for cup segmentation on the DRISHTI-GS1 test set. The method achieved a good glaucoma classification performance with an average AUC of 0.85 for five fold cross-validation on RIM-ONE v2.

Conclusions: We propose a method to jointly segment the optic disc and cup boundaries by modeling the drop in depth between the two structures. Since our method requires a single fundus image per eye during testing it can be employed in the large-scale screening of glaucoma where expensive 3D imaging is unavailable.

1. Introduction

Glaucoma, a chronic ocular disorder caused by the accelerated degeneration of the retinal optic nerve fibers, accounts for 12.3% of the total blindness world-wide [1] and projected to affect 79.86 million people by 2020 [2]. It results in a gradual loss of sight which starts with the peripheral vision and slowly progresses towards complete and irreversible vision loss. Due to its asymptomatic nature in the early stages, currently 70–90% of the glaucomatous population worldwide are reported to be unaware of their condition [3,4]. Large scale screening can play a vital role in preventing blindness through early detection and treatment.

Early diagnosis of glaucoma is primarily based on the assessment of structural changes in the optic disc (OD), though factors such as functional visual field assessment and intraocular pressure are also considered. OD is characterized by a bright elliptical region in the color fundus images. It contains a central depression called the optic cup (OC) which is surrounded by the neuro-retinal rim consisting of the retinal nerve fibers that bend into the OC (Fig. 1(a) and (b)). Loss of nerve fibers leads to rim thinning and a consequent enlargement of the OC. Several clinical measures such as the vertical Cup-to-Disc diameter ratio (CDR) and the ISNT rule based on the sector-wise rim thickness distributions [5], are used to quantify these structural changes. Automatic OD and OC segmentation can aid the measurement of such clinical indicators for an efficient and objective glaucoma assessment.

OC is primarily characterized by the depth information (Fig. 1 (b) and (c)). Topcon Imagenet and Humphrey Retinal Analyzers define the cup boundary at 125 μm and 120 μm below the OD edge [6] respectively. Several studies also define the cup edge at one-third or half drop in depth from the OD edge to the deepest point in optic cup [7–9]. In contrast to 3D imaging techniques such as Optical Coherence Tomography (OCT) and stereo fundus cameras that provide true depth estimation, monocular color fundus im-

* Corresponding author.
E-mail addresses: arunava.chakravarty@research.iiit.ac.in (A. Chakravarty), jsivaswamy@iiit.ac.in (J. Sivaswamy).

http://dx.doi.org/10.1016/j.cmpb.2017.06.004
0169-2607/

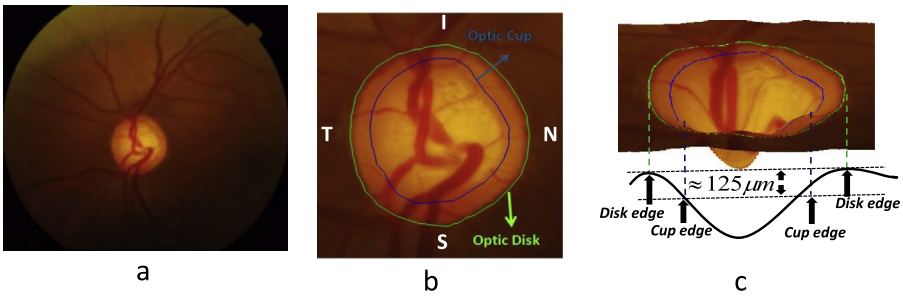

Fig. 1. (a) A color fundus image. (b) Cropped Region of interest of a. with optic disc and cup boundaries. (c) Topographical representation of b., cup boundary defined by the drop in depth from disc edge.

ages (CFI) are 2D projections of the retinal surface and lack explicit depth information. Though OCT and stereo imaging is widely used in hospitals, they cannot be employed in a large scale screening due to their cost and portability. In contrast, CFI is relatively inexpensive to acquire and widely available.

In this work we extend our prior work on OC segmentation [10] to jointly segment both OD and OC in a single optimization step. This is achieved by a novel, boundary-based CRF formulation which is effective in modeling the drop in depth between the OD and OC boundaries. In a clinical setting, both OCT and CFI are available for an eye, whereas during screening, only CFI is available. Hence, we employ a supervised depth estimation strategy to relate the appearance information from a CFI to corresponding depth estimates which requires only a single CFI image during testing.

2. Background

Majority of the existing methods segment OD first, followed by the OC in a sequential order. Since, OD segmentation is relatively easy compared to OC, more methods have been explored for the former.

OD segmentation: Techniques based on template matching, supervised classification, deformable and active shape models have been employed for this task. Template based methods often rely on the Hough Transform [11–13] to fit a circle or ellipse to the edge maps extracted from CFI. An alternative method is explored in [14] where the OD center is characterized by the maximum response of sliding bank filters applied at multiple scales and its boundary is obtained by smoothing the pixel locations that contribute to the maximum filter response. In the template based methods, the analysis is often restricted to the brighter regions in the image to improve the accuracy and efficiency [15]. For example, in [16], a two-step thresholding operation is applied to the image after enhancing the bright regions using iterative morphological operations. These methods suffer from inaccuracies due to the vessel occlusions in the OD region and inflexible shape assumptions. In [17], blood vessel inpainting is explored to handle the vessel occlusions followed by an adaptive threshold based region-growing technique for OD segmentation.

Deformable models such as Snakes [18], level sets [19], and the modified Chan-Vese model [20] improve on the template-based methods by iteratively refining the boundaries using energy minimization. The energy terms are often based on the image gradient computed in multiple color and feature channels. Recently, in [21] an active disc based deformable model has been explored. Active disc comprises a pair of concentric inner and outer discs corresponding to the OD boundary and a local background around it respectively, which is used to define a local contrast energy. These methods are sensitive to poor initialization which can be improved by combining multiple OD detectors through majority voting and data fusion [22]. Further, the gradient information is sensitive to ill-defined boundaries and the presence of peripapillary atrophy near the OD boundary. Active Shape Models in [23,24] incorporate a statistical shape prior. A set of landmark points on the OD is initialized using the mean shape from the training images and iteratively adapted to the test image, while being consistent with the point distribution model representing the shapes encountered during training.

Classification-based methods label each pixel [25], or superpixel [26] into OD or background classes using features such as Gaussian steerable filter responses on color opponency channels, disparity values extracted from stereo image pairs [25], color histograms and center-surround statistics [26]. Reliance on low level features make these methods susceptible to image noise and vessel occlusions. Moreover, the segmentations may contain multiple connected components.

OC segmentation: OC segmentation is restricted to the region inside OD. Since OC is largely characterized by a discontinuity in the depth of the retinal surface, proposed solutions either rely on explicit depth measurement or depth cues derived from appearance of the CFI. In the former approach, depth is obtained from OCT [27,28] or from stereo-based disparity maps [25,29,30]. Recently, in [31], information of Bruch's membrane opening from OCT is combined with fundus imaging for a joint multi-modal OD-OC segmentation. Factors such as cost, portability, and acquisition time (of OCT or stereo CFI) inhibit the widespread usage of these solutions in a large scale screening setting.

In monocular CFI, appearance of the pallor is characterized by the region of maximum color contrast within the OD and vessel bends as they enter into the cup. Using the pallor information alone [19,32] leads to inaccurate OC boundaries as a distinct pallor region is often absent. Moreover, while in normal cases, pallor and the OC boundary appear nearby, glaucomatous cases have a much larger cup encompassing the pallor [33]. Therefore, additional information based on vessel kinks (detected using wavelet transform or curvature information) have been employed in [20,34,35] to segment OC. Since a majority of blood vessels enter OC from the inferior and superior directions, boundary estimates in nasal and temporal sectors tend to be inaccurate. Further, only a small subset of locations where the vessels bend actually lie on the OC boundary, requiring several heuristics for selection of actual vessel kinks.

Supervised classification based methods have also been explored for OC segmentation [26]. A convolution neural network based method is explored in [36] where the filters are learnt over several layers. In [37], a supervised active shape model has been proposed. The initial boundary is represented by a set of landmark points which is iteratively refined using a cascade of regression functions. In each iteration, a separate regression function is learnt to map the image appearance features derived from the current boundary estimates to shape increment vectors which is used to refine the boundary.

Table 1
Dataset specifications. All datasets are publicly accessible except *Dataset* – 1.

Dataset	# images	Protocol	Camera	Source	Ground Truth	Evaluation
INSPIRE	30	4096 × 4096	Nidek 3Dx digital stereo	USA	OCT based depth	Depth Estimation
DRISHTI-GS1	50 train, 51 test	2896 × 1944 30° FOV	Zeiss Visucam NM/FA	India	Manual OD, OC marking	a) OD,OC segmentation b) CDR error
Dataset-1	28	2896 × 1944 30° FOV	Zeiss Visucam NM/FA	India	CDR from OCT & an expert marking	CDR error
RIM-ONE v2	455	cropped ROI around OD	Spain	image-level glaucoma diagnosis	Glaucoma classification	
DRIONS-DB	110	600 × 400 OD-centric,	digitized using HP-Photo Smart-S20	Spain	manual OD marking	OD segmentation
MESSIDOR	1200	1440 × 960, 2304 × 1536, 2240 × 1488, 45° FOV	Topcon TRC NW6	France	manual OD marking	OD segmentation

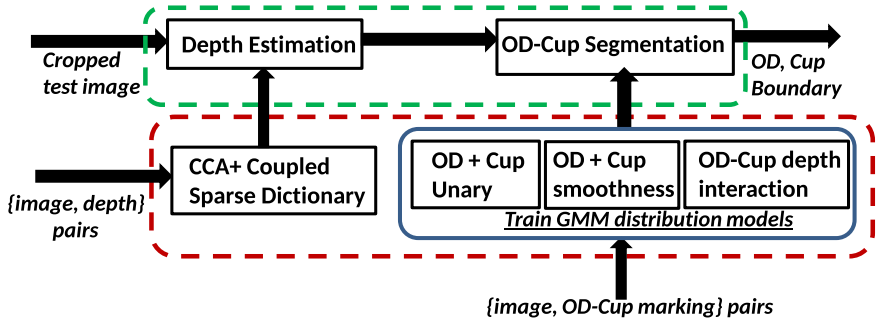

Fig. 2. Outline of the proposed system. Training(test) modules are enclosed within red(green) dotted box. (For interpretation of the references to color in this figure legend, the reader is referred to the web version of this article.)

3. Materials

The proposed method has been evaluated on six datasets: five publicly available, namely, INSPIRE [38], DRISHTI-GS1 [39], RIM-ONE v2 [40], DRIONS-DB [41] , MESSIDOR [42] and a privately collected dataset referred to as DATASET-1. The datasets cover a range of ethnicity in population, imaging protocols, fundus cameras and image quality. Comprehensive experiments were performed aimed at testing the segmentation and its use in glaucoma diagnosis. Depending on the availability of Ground Truth (GT), different evaluation criterions were used for each dataset. A summary of each dataset and the experiments performed on them is provided in Table 1.

GT for MESSIDOR is available from University of Huelva [43] which has been used to benchmark several OD segmentation algorithms [13,44,45].

The locally sourced Dataset-1 contains 18 normal and 10 glaucomatous images acquired from Aravind Eye Care Hospital, Madurai, India for which both CFI and OCT imaging is available. The CDR in the OCT generated report of corresponding fundus images was taken as the gold standard. Structural markings of OD-OC boundaries by an expert was also collected for comparison.

Images in all datasets are OD-centric with the exception of MESSIDOR that provides macula-centric images. DRIONS-DB contains challenging cases such as illumination artefacts, blurred or missing rim, peripapillary atrophy and strong pallor distractor [46]. The INSPIRE dataset provides normalized ground-truth depth maps for each CFI obtained using manual layer segmentation and registration of corresponding 3D-OCT images.

4. Methods

A rough region of interest (ROI) is extracted from the given CFI during pre-processing and provided as input to the proposed method for joint OD-OC segmentation. The ROI extraction is discussed in Section 4.1. Our proposed method depicted in Fig. 2. consists of 2 stages: (i) Supervised depth estimation from the input ROI; (ii) extraction of OD-OC boundaries using the depth estimates and color gradients extracted from the ROI.

To estimate depth, Canonical Correlation Analysis (CCA) and coupled sparse dictionary (CSD) basis are learnt from a set of CFI-depth map pairs during training to relate image appearance to depth values. The learnt basis vectors are used during testing to estimate the depth from CFI images alone. The details are provided in Section 4.2.

The proposed CRF formulation for the joint OD-OC segmentation is presented in Section 4.3. Its various energy terms model the expected distribution of the color gradients and relative drop in depth between the OD and OC boundaries. The probability distributions are learnt from a separate set of training CFI images with manual OD and OC markings from experts.

4.1. ROI extraction

A Hough transform based algorithm based on [20] is used to localise the OD region. First, the candidate regions for OD are identified by thresholding the red channel of the CFI at 0.95 after normalizing it to [0,1]. Thereafter, the vessels are supressed within the selected candidate regions using morphological top-hat operation on the green channel to obtain a rough vessel mask followed by a diffusion based inpainting [47]. Next, an edge map is extracted by applying Canny edge detector at a very low threshold. Circular Hough transform is employed to obtain a rough estimate of the OD center and radius R. Finally, a square region of interest (ROI) of size $3R$ (with a margin of $0.5R$ on all sides) is extracted (see Fig. 1(a) and (b)).

4.2. Supervised depth estimation

The proposed depth estimation pipeline is depicted in Fig. 3. Initially, two separate estimates of depth denoted by d_l and d_c are derived from the luminance and chrominance features respectively. While d_c is obtained by relating the color features at each pixel

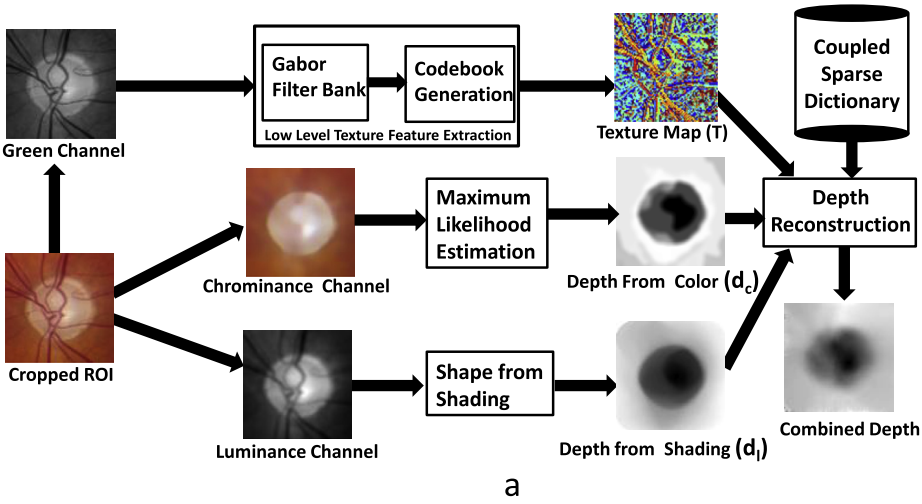

Fig. 3. Overview of the proposed supervised depth estimation method.

to probable depth values, d_l is derived from the intensity (gray-scale) image using an unsupervised shape from shading (SFS) algorithm. The details of extracting d_l and d_c are discussed below in Sections 4.2.1 and 4.2.2 respectively. Finally, d_l and d_c are integrated at a patch level along with Gabor filter-bank based texture features and mapped to ground-truth (GT) depth values using coupled sparse dictionary (CSD). The details of the patch level feature extraction in the appearance and depth feature spaces is described in Section 4.2.3 followed by the details of the CSD based mapping in Section 4.2.4.

4.2.1. Depth estimation from luminance

The luminance channel L is obtained as the average of the R,G and B channels of the color fundus image ROI followed by the suppression of the high color gradients using the method in [48]. The depth estimate d_l is obtained from L using the simple but fast unsupervised shape from shading algorithm in [49]. Some simplistic assumptions are made to have a tractable solution: (i) retinal surface is assumed to be Lambertian. (ii) The albedo (surface reflectivity) of the retinal surface is uniform. Since albedo of blood vessels is different from that of the retinal surface, vessel inpainted images obtained during ROI extraction are used. (iii) The albedo and illumination direction is computed from the image itself following the method in [50] under the assumption that the surface normals are distributed evenly in the 3D space. Since, the SFS algorithm implicitly assumes bright regions to be closer to the camera, the complement of its output gives the actual depth estimate. Though an exact reconstruction of depth from a single view is not possible due to the simplified assumptions made in the SFS algorithm, results (Section 5.1) indicate a strong positive correlation between d_l and the true depth values.

4.2.2. Depth estimation from chrominance

The mean and variance of each of the R, G, B color channels of the vessel inpainted ROI in the fundus image is first standardized to fixed values (the average values computed from the INSPIRE dataset) and then normalised ($j/(r+g+b)$; $j = r, g, b$) to obtain a 3-long illumination invariant color feature C for each pixel. The color-based depth estimate d_c is obtained from C using a supervised approach: for each depth value $d \in [0, 255]$, the conditional $P(C|d)$ is learnt from a training set of image-depth pairs, using a GMM with number of Gaussians selected in the range 1–6 that maximizes the Akaike information criterion (AIC) [51]. During testing, the maximum a posteriori estimate for $P(d|C)$ is computed. The lack of one-to-one correspondence between the color and depth values and treating each pixel independent of its neighborhood leads to inaccuracies in the d_c estimates.

4.2.3. Patch-level feature extraction

To obtain a robust and accurate depth estimate, d_l and d_c are integrated at a patch level along with texture features to obtain the final depth estimate. Each 8×8 image patch at location i is represented by a 444 dimensional appearance feature p_i extracted from the fundus image and a 192 dimensional depth feature q_i extracted from the corresponding patch in the GT depth map derived from OCT. While both image and the corresponding GT depth map d_{oct} is available during training, only fundus image is available during testing. The goal is to learn a mapping between the two feature spaces to predict the depth feature of a patch given its appearance feature.

To obtain the appearance feature, at first each pixel in the image patch is represented by a 6-D appearance feature f_a obtained by concatenating d_l, d_c and their gradients $\frac{\partial d_l}{\partial x}$, $\frac{\partial d_l}{\partial y}$, $\frac{\partial d_c}{\partial x}$, $\frac{\partial d_c}{\partial y}$. The ith patch in a CFI is represented by a vector $p_i \in R^{444}$ obtained by concatenating f_a of all 64 pixels in the patch and a 60-bin histogram of a texture word map T within the patch.

T is extracted from the green channel of the fundus image. Each pixel is represented by the responses of a gabor filter bank comprising of 36 filters along with their 1st and 2nd order derivatives in the two directions resulting in a $(36 \times (1+2+2) = 180$-long feature which is clustered (during training) into 60 words. Each pixel is then represented by the nearest word index [52] to obtain T. The filter bank consists of gabor filters in 6 orientations ($\{0, 30, 60, 90, 120, 150\}$ degrees) at 6 scales ($\sigma = \{0.04 \times 1.6^s \mid 1 \le s \le 5, s \in Z\}$) with the aspect ratio and wavelength fixed at 0.5 and $\frac{\sigma}{0.56}$ respectively.

The depth feature is obtained by representing each pixel location by a 3-D depth feature vector f_d obtained by concatenating the GT depth d_{oct} along with it's gradients $\frac{\partial d_{oct}}{\partial x}$, $\frac{\partial d_{oct}}{\partial y}$. A patch-level aggregation of f_d results in the depth feature $q_i \in R^{192}$.

The publicly available INSPIRE dataset [38] is used to train our depth estimation method which provides the corresponding depth map d_{oct} for each fundus image as the GT. In INSPIRE, the depth maps were computed by additionally collecting the 3D OCT images corresponding to each fundus image. The depth of the retinal surface was extracted from the OCT and manually registered to the fundus image.

Thus, M image patches, are represented in the appearance and depth space by matrices P and Q whose M columns are p_i and q_i,

respectively. The patch features yield a more robust representation relative to the individual pixel-level depth estimates. The dimensionality of P and Q is jointly minimized by employing CCA [53]. CCA projects both P and Q into two separate 192-D feature spaces. In contrast to other dimensionality reduction techniques such as PCA which can be applied to each feature space independently, CCA jointly computes a pair of basis $\phi_{img} \in R^{444 \times 192}$ and $\phi_{depth} \in R^{192 \times 192}$ for the two feature spaces such that for each image patch, the correlation between its appearance and the depth feature is maximized. ϕ_{img} and ϕ_{depth} projects P and Q to $P_{cca} = \phi_{img}^T.P$ and $Q_{cca} = \phi_{depth}^T.Q$ respectively. The dimensionality reduction in the appearance features from 444 to 192 helps to reduce the risk of overfitting on the training data as well as decreases the memory and computational requirements for learning the coupled sparse dictionaries. The dimensionality of the depth features in Q is not reduced in Q_{cca} to enable an exact reconstruction of the depth feature vector using the inverse of the ϕ_{depth} basis.

4.2.4. Coupled sparse dictionary

The task of predicting a 192-D depth feature from the corresponding appearance feature is a multi-output regression problem. Therefore, the regression based methods that predict a single output are unsuitable for this purpose. CSD provides a way to model such mappings and has been shown to be effective in applications such as image super-resolution where the image patches in a low resolution are mapped to the corresponding image patches in the high resolution [54].

Majority of the sparse dictionary learning methods focus on training an over-complete dictionary in a single feature space for various signal recovery and recognition tasks such as image impainting [55], face recognition [56] and object tracking [57]. In contrast, the CSD considers two feature spaces which in our case are the appearance and the depth feature spaces respectively. The unknown mapping function between them is modeled by jointly learning a separate over-complete dictionary in each feature space such that the sparse representation of a feature in the appearance space can be used to reconstruct its paired feature in the depth space [54].

Let U and V denote the two overcomplete CSD, each with 1100 dictionary atoms, in the P_{cca} and Q_{cca} feature space respectively. The sparse code α is shared in the two representations: $P_{cca} \approx U.\alpha$ and $Q_{cca} \approx V.\alpha$ for all the training patches. Hence, estimation of U, V is posed as

$$argmin_{U,V,\alpha} \parallel P_{cca} - U.\alpha \parallel_2 + \parallel Q_{cca} - V.\alpha \parallel_2 + \lambda. \parallel \alpha \parallel_0 . \quad (1)$$

E.q. 1 can be rewritten by concatenating P and Q resulting in the standard sparse dictionary learning problem [54] which can be formulated as

$$argmin_{U,V,\alpha} \left\| \begin{bmatrix} P_{cca} \\ Q_{cca} \end{bmatrix} - \begin{bmatrix} U \\ V \end{bmatrix} .\alpha \right\|_2 + \lambda. \parallel \alpha \parallel_0 . \quad (2)$$

An online dictionary learning algorithm [58] was used for learning the sparse dictionary $\begin{bmatrix} U \\ V \end{bmatrix} \in R^{384 \times 1100}$ from the feature set $\begin{bmatrix} P_{cca} \\ Q_{cca} \end{bmatrix}$ using a batch size of 600, sparsity coefficient $\lambda = 0.6$ and max-iteration= 800. The learnt basis is split horizontally to obtain U and V.

Coupled Sparse Dictionary Testing: The given test image ROI is densely sampled into overlapping patches which are represented in the patch level image space by P_{test}. The sparse code α^* is estimated by solving the LASSO optimization problem,

$$\alpha^* = argmin_\alpha ||U.\alpha - P_{test}||_2^2 \quad s.t. \quad ||\alpha||_1 \leq \lambda. \quad (3)$$

The corresponding estimated depth in CCA space, Q_{est} is then obtained by projecting α onto the depth basis V using

$$Q_{est} = V.\alpha^*. \quad (4)$$

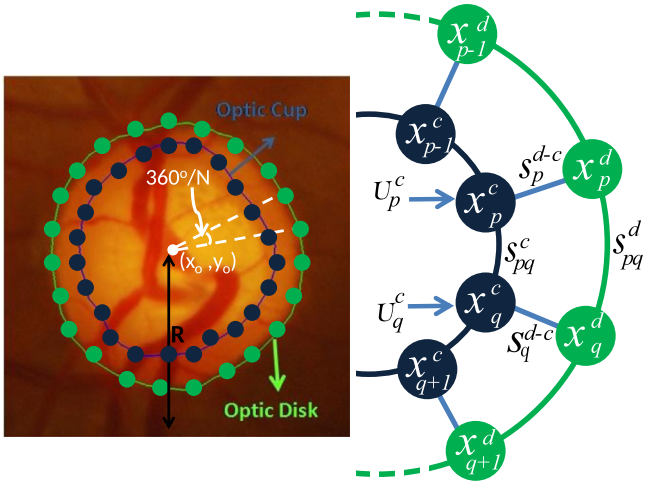

Fig. 4. The parameterization and graphical model representation of OD-OC boundaries.

Q_{est}, is backprojected onto the CCA basis to obtain $D_{est} = (\phi_{depth})^{-1}.Q_{est}$, which consists of the depth value d and its gradients $\frac{\partial d}{\partial x}$ and $\frac{\partial d}{\partial y}$ at each pixel. The refined depth value is taken as the average of d and the depth estimated from $\frac{\partial d}{\partial x}$ and $\frac{\partial d}{\partial y}$ using gradient inversion method in [48]. Thus, having estimated the depth map for a given CFI, next, we present details on how it is used to segment the OD and OC.

4.3. Joint OD-OC segmentation

The proposed joint segmentation framework seeks to extract both the OD and OC boundaries from a given image ROI by formulating it as a CRF based energy minimization problem. The OD and OC boundaries are modeled as concentric closed curves about the *ROI* centre denoted by O: (x_o, y_o). The two curves are parameterized by N points uniformly spaced in orientation which are represented in the polar coordinates by $(x_n^i, \theta_n), n \in \{1, 2, \ldots, N\}$. Here x_n^i represents the radial distance of the nth point from O, $\theta_n = (n-1) \times \frac{360^\circ}{N}$ represents its angular orientation with respect to the horizontal and $i \in \{d, c\}$ represents points on the OD and OC boundary respectively.

Each x_n^d and x_n^c is a discrete random variable that can take values from the label set $L = \{l | 1 \leq l \leq R, l \in Z^+\}$, where R represents the radius of the largest circle that can be enclosed within the *ROI* and Z^+ is the set of all positive integers. The set of random variables $X = \{x_n^d, x_n^c\}_{n=1}^N$ defines a Random Field and $\mathbf{x} \in L^{2N}$ denotes a feasible labeling of X obtained by assigning a label from L to each x_n^i. The graphical model corresponding to X is depicted in Fig. 4, where each node belonging to OD and OC correspond to the random variables x_n^d, x_n^c and are color coded green and blue, respectively.

For each random variable x_n^d, a Disc unary term $U_n^d(x_n^d = l)$ is defined to capture the probability that the OD boundary passes through the point $(l, (n-1) \times \frac{360^\circ}{N})$, given a set of features that capture the gradient characteristics of OD boundary at that point. An identical set of features is used to define the Cup Unary term $U_n^c(x_n^c = l)$ which captures the pallor gradient at cup boundary.

Moreover, based on the Markovian assumption, the label of each x_n^i is also considered to be dependent on its immediate neighbors in the same as well as the adjacent boundary. The smoothness of the OD and OC boundary is captured by the disc and cup smoothness energy terms denoted by $S_{p,q}^d(x_p^d, x_q^d)$ and $S_{p,q}^c(x_p^c, x_q^c)$ respectively. They are defined between each pair of adjacent nodes

(p, q) lying in the OD or OC boundary. A disc-cup interaction term $S_n^{d-c}(x_n^d, x_n^c)$ is defined between the corresponding nodes across the two boundaries that lie in the same orientation to capture the relative drop in the depth between the OD and OC boundaries. Thus, the CRF energy $E(X)$ is defined as

$$\begin{aligned} argmin_{\mathbf{x}} E(\mathbf{x}) = &\sum_{n=1}^{N} U_n^d(x_n^d) + \lambda_1 \sum_{p,q \in N_d} S_{p,q}^d(x_p^d, x_q^d) \\ &+ \lambda_2 \sum_{n=1}^{N} U_n^c(x_n^c) + \lambda_3 \sum_{p,q \in N_c} S_{p,q}^c(x_p^c, x_q^c) \\ &+ \lambda_4 \sum_{n=1}^{N} S_n^{d-c}(x_n^d, x_n^c), \end{aligned} \tag{5}$$

where N_d and N_c represents the set of adjacent pair of nodes in the OD and OC boundaries respectively and defined as $N_i = \{(x_k^i, x_{mod(k,N)+1}^i) | 1 \le k \le N\}$. The labeling $\mathbf{x}$ that maximizes $E(\mathbf{x})$ corresponds to the desired segmentation. During implementation, e.q. 5 is solved using the Sequential Tree-Reweighted Message Passing algorithm in [59]. The details of the various energy terms are described below.

Disc and cup Unary Terms: We denote the probability that the pixel at a distance of l in the direction θ_n lies on the OD and OC boundary by $P_n^d(\vec{f}_{n,l})$ and $P_n^c(\vec{f}_{n,l})$ respectively. The feature $\vec{f}_{n,l}$ extracted at each pixel, consists of the color gradients *computed along the radial direction* θ_n in a 31 × 31 neighborhood in *R of RGB, V of HSV, and all 3 color channels in YCbCr color space* respectively. The gradient values along each radial direction are further normalized to [0,1]. Since, $E(X)$ is to be minimized, we define the unary terms $U_n^d(x_n^d = l)$ and $U_n^c(x_n^d = l)$ to be inversely related to the probability as

$$\begin{aligned} &U_n^d(x_n^d = l) = 1 - P_n^d(\vec{f}_{n,l}) \text{ and} \\ &U_n^c(x_n^c = l) = 1 - P_n^c(\vec{f}_{n,l}). \end{aligned} \tag{6}$$

Smoothness terms: The smoothness terms S^d and S^c are defined using the probability distribution function (pdf) of the distance between the adjacent boundary points as

$$\begin{aligned} &S_{p,q}^d(x_p^d = l, x_q^d = m) = 1 - P_d^{(p,q)}(|\, l - m \,|) \text{ and} \\ &S_{p,q}^c(x_p^c = l, x_q^c = m) = 1 - P_c^{(p,q)}(|\, l - m \,|). \end{aligned} \tag{7}$$

$P_d^{(p,q)}$ and $P_c^{(p,q)}$ represents the pdf of the spatial variation in the adjacent nodes, $(x_p^d, x_q^d) \in N_d$ and $(x_p^c, x_q^c) \in N_d$ on OD and OC boundary respectively.

Disc-Cup interaction term: This pairwise term captures the relationship between corresponding landmark points on the disc x_n^d and the cup x_n^c along θ_n. A radial profile of length R is extracted from the estimated depth map D along θ_n and normalized in the range [0, 1] such that the deepest point has a depth of 1. Rather than using an empirical ratio for the drop in depth (for e.g., one-third was used in [29]), we learn its pdf (one for each direction) from the training data. Thus, the disc-cup interaction term is defined as

$$S_n^{d-c}(x_n^d, x_n^c) = \begin{cases} 1 - P_n^d(D(x_n^d) - D(x_n^c)), & \text{if } x_n^d \ge x_n^c \\ \infty, & \text{otherwise,} \end{cases} \tag{8}$$

where P_n^d models the drop in depth $D(x_n^d) - D(x_n^c)$ between OD and cup boundary in the nth direction. Configurations in which the radial distance of cup landmark x_n^c exceeds that of the corresponding disc landmark x_n^d are infeasible because OC always lies within the disc. This is ensured by assigning ∞ to such disc-cup interaction terms.

The pdfs in Eqs. (6)–(8) are modeled independently using separate GMMs (multivariate, in the case of unary terms) and learnt from expert-marked OD and OC boundaries in the training images using Expectation-Maximization. The optimal number of Gaussians in the GMMs are selected by maximizing the Akaike Information Criterion [51] by searching in the range between 1 and 5.

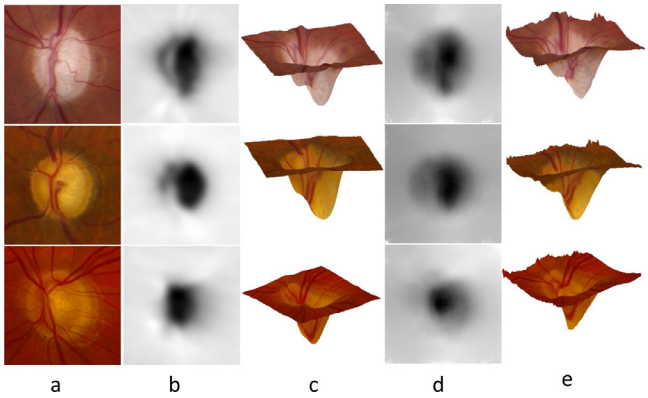

Fig. 5. OD regions from 3 sample images (column a). Corresponding depth estimates are shown as greysacle image and topographical maps with input image wrapped onto depth surface. Columns b and c are ground truth; Columns d and e are computed results.

5. Results

The supervised depth estimation method is evaluated in Section 5.1. Various experiments to evaluate the joint OD-OC segmentation is presented in Section 5.2. This includes a *comparison with other state of the art* methods (5.2.2); errors in computed *CDR* (5.2.3) and the *rim thickness error across sectors* (5.2.4). The utility of the segmentation in *glaucoma detection* is evaluated in Section 5.3.

5.1. Evaluation of depth estimation

Since, OC boundary is primarily defined by the *relative* drop in depth values, depth maps defined up to an arbitrary scale factor contain sufficient information for cup segmentation. Moreover, the ground-truth depth maps in the INSPIRE dataset used in our evaluation are normalized to [0,255]. Hence, *Pearson product-moment correlation coefficient* ρ is used for assessment. $\rho \in [-1, 1]$ where -1 (or 1) indicates a total negative (or positive) correlation while 0 indicates no correlation. It is defined as

$$\rho(d, D) = \frac{\sum_m \sum_n (d_{m,n} - \bar{d})(D_{m,n} - \bar{D})}{\sqrt{(\sum_m \sum_n (d_{m,n} - \bar{d}))^2 (\sum_m \sum_n (D_{m,n} - \bar{D}))^2}}, \tag{9}$$

where d (or D) denotes the computed (or GT) depth map with mean $\bar{d}$ ($\bar{D}$) and m, n denote pixel locations. Due to a limited data availability, Leave-One-Out cross-validation was employed for evalutation, using 29 images to train and 1 image to test in each fold. Qualitative results are depicted in Fig. 5 where darker pixels in the 2nd and 4th columns indicate higher depth values. Depth estimation using SFS alone performs better than mapping color intensities directly to corresponding depth values using GMM with a mean/std. ρ of 0.76/0.13 and 0.72/0.13 respectively. The proposed method which combines cues from SFS, GMM based depth from color and texture features by the coupled training further improves the depth estimation with a ρ of 0.80/0.12.

The proposed CSD based method was benchmarked against L2-normalized ridge regression that maps the appearance features to corresponding depth values at the central pixel location in each patch. The method resulted in a ρ of 0.77/0.14 in comparison to 0.80/0.12 obtained by the proposed method. The better performance of the CSD based method can be attributed to the fact that

Table 2
Segmentation performance on DRISHTI-GS1.

Method	Training				Testing			
	OD		Cup		OD		Cup	
	Dice	BLE	Dice	BLE	Dice	BLE	Dice	BLE
Sequential approaches								
Vessel Bend [20]	0.96/0.05	8.61/8.89	0.74/0.20	33.91/25.14	0.96/0.02	8.93/2.96	0.77/0.20	30.51/24.80
Superpixel [26]	0.95/0.04	9.39/6.81	**0.84/0.12**	**16.89/8.1**	0.95/0.02	9.38/5.75	0.80/0.14	22.04/12.57
Multiview [60]	0.96/0.05	8.61/8.89	0.77/0.17	24.24/16.90	0.96/0.02	8.93/2.96	0.79/0.18	25.28/18.00
Joint approaches								
Graph cut prior [61]	0.93/0.06	12.94/11.67	0.76/0.15	29.65/ 18.01	0.94/0.06	14.74/15.66	0.77/0.16	26.70/16.67
Proposed	**0.97/0.02**	**6.42/3.36**	**0.84/0.14**	17.44/12.80	**0.97/0.02**	**6.61/3.55**	**0.83/0.15**	**18.61/13.02**

it allows a richer representation of the depth feature space consisting of depth values as well as its gradients that capture the local variation at a patch level.

5.2. Evaluation of OD-OC segmentation

5.2.1. Evaluation metrics

Both region and boundary localization based metrics are used to evaluate the segmentation results. *Dice* similarity coefficient $D(X, Y)$ measures the extent of overlap between the set of pixels in the segmented region X and ground truth Y and can be defined as

$$D(X,Y) = \frac{2.\mid X \cap Y \mid}{\mid X \mid + \mid Y \mid}. \tag{10}$$

Since Dice coefficient is unsuitable to gauge the segmentation performance at a local (boundary) level, the average *boundary distance localization error* (*BLE*) is also employed to measure the distance (in pixels) between the computed (C_o) and GT (C_g) boundaries. It is defined as

$$BLE(C_g, C_o) = \frac{1}{n}\sum_{\theta=1}^{\theta_n} \mid r_\theta^g - r_\theta^o \mid, \tag{11}$$

where r_θ° (r_θ^g) denotes the radial euclidean distance of the estimated (GT) boundary point from the centroid of the GT in the direction θ; 24 equi-spaced points were considered in the evaluation. The desirable value for *BLE* is 0.

5.2.2. Benchmarking against state of the art

The segmentation performance of the proposed method was compared with 4 other methods on DRISHTI-GS1. Sample qualitative results are shown in Fig. 6. Quantitative results are presented in Table 2. The best figures for Dice and BLE are shown in bold fonts. The proposed method is seen to achieve the best figures consistently. The exception is [26] which achieves the best figures for OC segmentation on the training set, which however, degrades on the Test set. The high dimensionality (1025) feature-based superpixel method [26] tends to overfit the training data. The next best-performing method is the depth-based method in [60]. This however, requires two CFIs per eye (during train and test phase) unlike our method which requires single CFI per eye during testing, thus, providing significant advantage. [61] also adopts a joint OD-OC segmentation framework but treats it as a pixel labeling problem. It requires direct edges in a 15 pixel neighborhood for each pixel and doesnot consider depth information. In contrast, the proposed method uses a *boundary based* formulation requiring labeling of only 72 landmark points and lends a natural way to model the depth-based inter-dependence between OD and OC by 36 edges (OD-cup interaction term) resulting in improvement in speed as well as accuracy as seen in the results of [61] on DRISHTI-GS1 in Fig. 6 and Table 2.

Table 3
Optic disc segmentation performance on DRIONS-DB. (mean/std).

	Dice	BLE
Walter et al. [63]	0.68/0.39	_
Morales et al. [62]	0.88/0.17	_
Morales et al. [46]	0.91/0.10	_
Proposed Method	0.95/0.03	2.27/1.24
Expert 2	0.96/0.03	2.11/1.13

Table 4
Optic disc segmentation performance on MESSIDOR. (mean/std).

	Jaccard	BLE
Morales et al. [46]	0.82/0.14	_
Yu et al. [45]	0.84	_
Roychowdhury et. al. [15]	0.84	_
Aquino et al. [13]	0.86	_
Marin et al. [16]	0.87	_
Giachetti et al. [44]	0.88	_
Proposed Method	0.87/0.22	4.32/4.71

Our method also outperforms the recent methods in [21,36] on OD segmentation and is comparable to [36] on the OC segmentation task. The unsupervised active disc energy based method in [21] reported a dice of 0.91 for OD on the combined training and test set of DRISHTI-GS1. The deep convolution network based method in [36] achieved a dice coefficient of 0.95 for OD and 0.83 for OC respectively using a five fold cross-validation on the training set of DRISHTI-GS1. While the performance of [36] for OC segmentation is comparable to our method on the training set, its performance on the test set is not available for comparison.

The OD segmentation results of the proposed method has also been reported on DRIONS-DB in Table 3 and MESSIDOR in Table 4. Though the proposed method jointly computes both OD and OC segments, the accuracy of OC could not be evaluated on these datasets in the absence of ground truth cup markings. The results reported in [13,15,16,44–46,62,63] have been reproduced in Tables 3 and 4 to benchmark the performance of the proposed method. While Dice coefficient was used as the region-based metric for DRIONS-DB, Jaccard similarity coefficient J was used for MESSIDOR following the norms of the previously published results for a direct comparison. J also measures the extent of overlap between the set of pixels in the segmented region X and ground truth Y as

$$J(X,Y) = \frac{\mid X \cap Y \mid}{\mid X \cup Y \mid}. \tag{12}$$

On DRIONS-DB, the proposed method outperforms the state of the art and performs comparably to human experts, while in MESSIDOR, the performance is comparable to other state of the art methods.

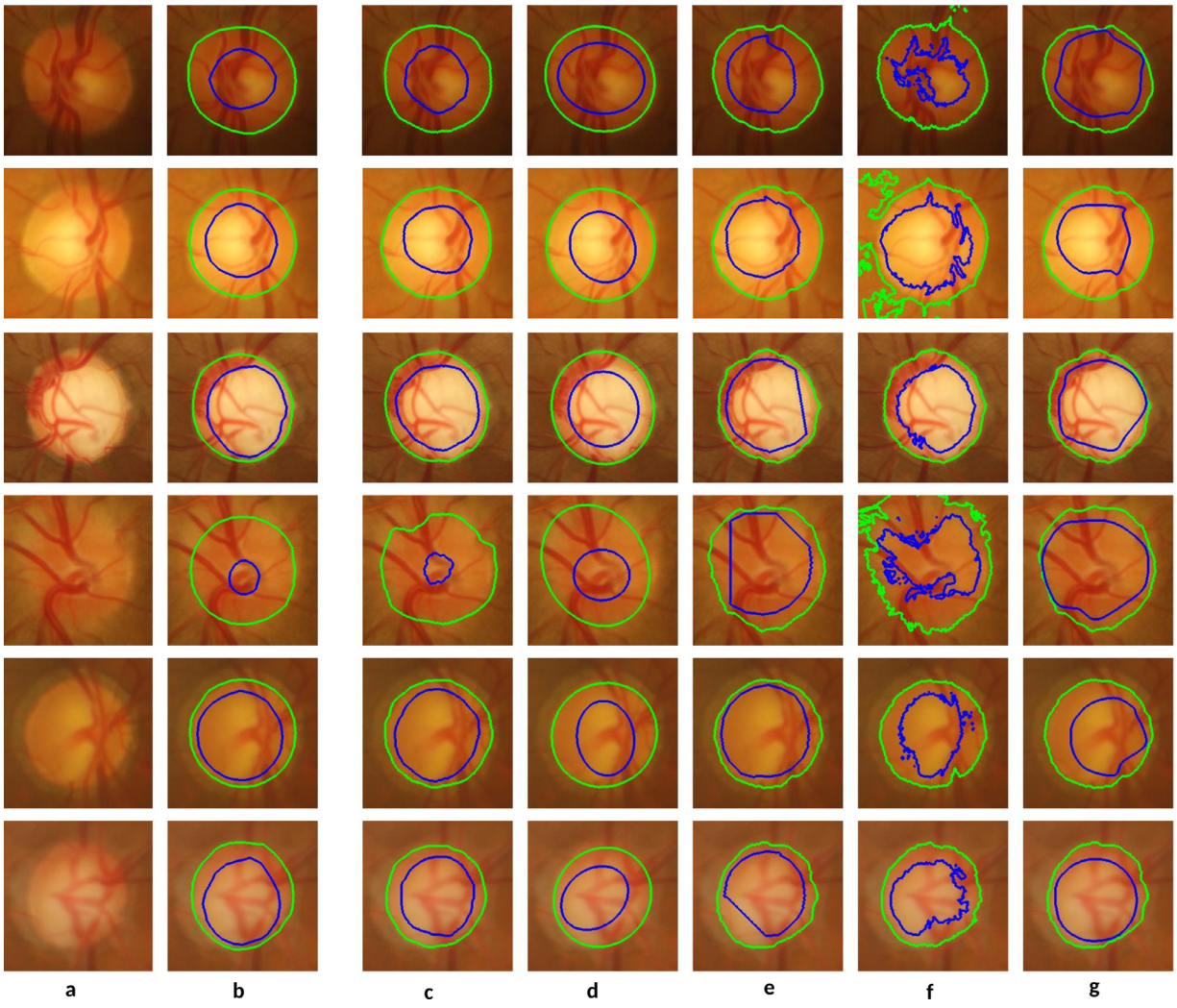

Fig. 6. Qualitative results on some challenging cases. Disc and cup boundaries are depicted in green and blue respectively. (a) cropped region around OD; (b) Ground Truth; Results of (c) Proposed Method; (d) Superpixel based [26]; (e) Multiview [60] (f) Graph Cut prior [61] (g) Vessel bend [20]. (For interpretation of the references to color in this figure legend, the reader is referred to the web version of this article.)

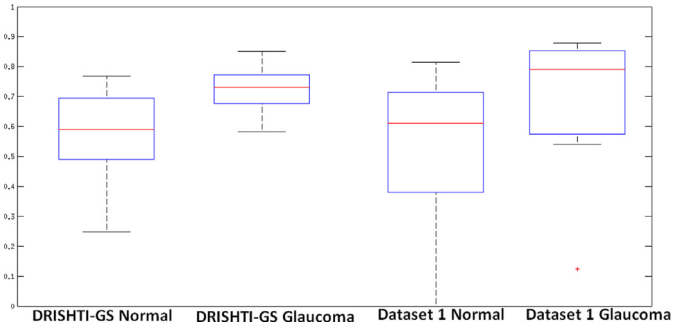

Fig. 7. Box and whisker plots of the distribution of CDR values estimated with the proposed method.

Table 5
CDR errors (mean/std.) for the proposed method.

	Normal	Glaucoma	Combined
	DRISHTI-GS1 Train Set		
Proposed Method	0.11/0.11	0.07/0.05	0.08/0.08
	DRISHTI-GS1 Test Set		
Proposed Method	0.14/0.15	0.06/0.05	0.08/0.09
	Dataset-1		
Proposed Method	0.16/0.19	0.16/0.24	0.16/0.20
Expert 1	0.05/ 0.03	0.03 / 0.03	0.04/ 0.03

5.2.3. CDR analysis

Vertical CDR is a key metric widely used in clinical assessment of glaucoma. The proposed method was evaluated on 2 datasets: DRISHTI-GS1 and Dataset-1. For Dataset 1, corresponding OCT reports were also available and used as Gold standard. The range of estimated CDR values is plotted in Fig. 7. While the median CDR values for the 2 classes are well separated (0.6 versus 0.75), for both datasets, the standard deviation is higher for Dataset-1. While a clear separation between the 2 classes cannot be obtained from the estimated CDR alone, it can act as a useful feature in automated glaucoma classification. The mean and standard deviation of absolute error in estimated CDR are listed in Table 5. The proposed method had an overall mean error of 0.08 in DRISHTI-GS1 which increases to 0.16 when compared to OCT based Gold standard in Dataset-1. In comparison, human experts achieved a better estimate of CDR against the Gold standard with a mean error of 0.04.

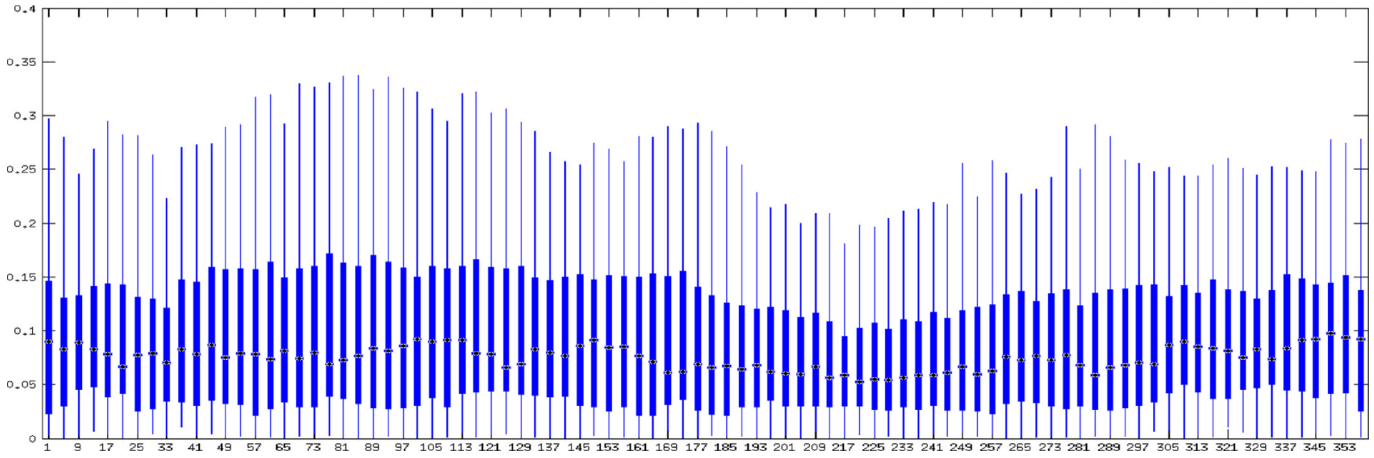

Fig. 8. Rim thickness error distribution across all sectors.

5.2.4. Analysis of rim thickness

The distribution of the overall rim thickness along all sectors of OD also plays an important role in glaucoma diagnosis. Rim thickness ratio (RTR) is defined as the ratio of cup radius to disc radius along different orientation angles about the OD center. The absolute error in RTR between the estimated and GT segmentations was evaluated. The overall mean/std. in RTR error was 0.102/0.098 for the Test set and 0.096/0.094 for Training set of DRISHTI-GS1 across all orientations. Fig. 8. depicts the distribution of RTR error across 360° , 4° apart. The smooth trend indicates a lack of regional bias in rim thickness error as opposed to vessel-kink based methods which tend to be more erroneous in the nasal and temporal regions due to absence of vessels in these sectors.

5.3. Glaucoma screening

The utility of our segmentation method in the detection of glaucoma was evaluated on RIM-ONE v2. The OD-OC segmentations for the 455 images in RIM-ONE was obtained by training the proposed system on DRISHTI-GS1. Thereafter, a 14D feature was extracted from the segmentations: (a) vertical CDR and rim to disc area ratio; (b) vertical OD diameter; (c) ratio of horizontal to vertical CDR (d) 6 features computed by $\frac{r_i - r_j}{\sigma_i + \sigma_j}$ with $i \neq j$ and $(i, j) \in \{(I, S, N, T)\}$; e) $\sigma(r_k)$with $k \in \{I_N, I_T, S_N, S_T\}$ to capture local deformations in these sectors. *I, S, N* and *T* represents the Inferior, Superior, Nasal and temporal sectors of OD (see Fig. 1(a)), which are further subdivided into Inferio-nasal (I_N), inferio-temporal (I_T), superio-nasal (S_N), superio-temporal (S_T) quadrants. The mean and standard deviation of the rim thickness between the OD and OC boundaries are denoted by r_i and σ_i respectively. A five fold cross-validation was performed using SVM with RBF kernel as the classifier. *The system achieved an average area under the curve (AUC) of* 0.85 ± 0.04 *and an average accuracy of* 0.77 ± 0.02. *AUC decreases to* 0.71 ± 0.03 *with only CDR, indicating that accurate segmentation in all sectors is critical to improve the classification performance*. The ROC curves of the 5 folds is shown in Fig. 9.

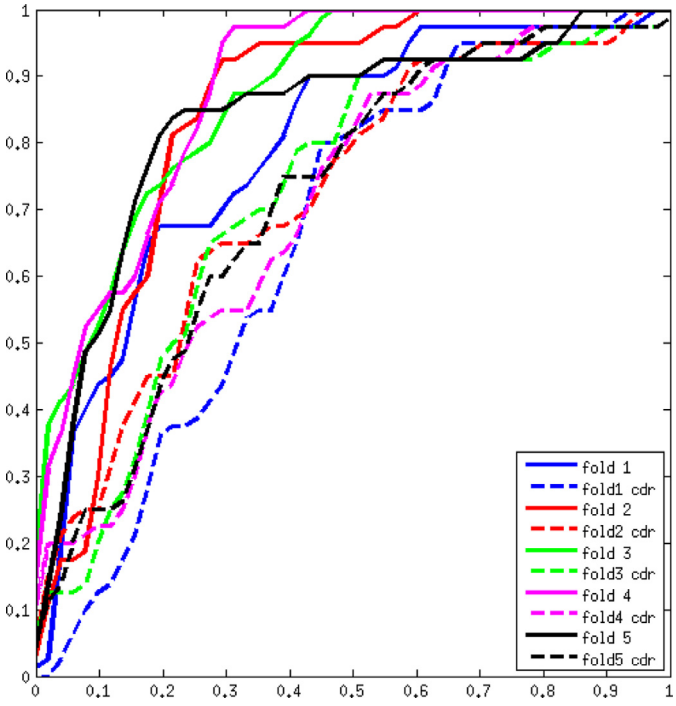

Fig. 9. ROC curves of glaucoma classification on RIM-ONE v2 for five fold cross-validation. Solid and Dotted lines indicate performance obtained using 14-D feature and CDR alone respectively.

6. Discussion

In this work, a joint boundary based OD-OC segmentation formulation is proposed that explicitly models the drop in depth between the two boundaries. In the absence of true depth in 2D color fundus images, a supervised method is employed to estimate the depth from the image appearance. The proposed method outperformed several existing methods on the task of OC segmentation in the DRISHTI-GS1 dataset. For OD segmentation, the proposed method outperformed the existing methods on DRIONSDB and DRISHTI-GS1, while the performance was comparable to the state of the art on the MESSIDOR dataset. However, in terms of error in CDR estimates, a human expert was found to surpass our method's performance against the OCT based Gold standard, indicating a scope for further improvement. An analysis of the rim-thickness error across all directions did not indicate any sector-wise regional bias in the segmentation accuracy. A set of features extracted from the OD-OC segmentation was able to achieve an AUC of 0.85 on the task of glaucoma classification on the RIM-ONE dataset indicating the potential use of the proposed method in glaucoma screening.

The proposed method has been implemented in Matlab and it takes an average of 9.3 s per image to obtain OD and OC segmentations on a 3 Ghz, i7 processor with 8GB RAM. The parameters λ_1, λ_2, λ_3 and λ_4 in Eq. (5) control the relative weights of the unary,

Table 6
Analysis of Energy terms: λ_1, λ_2, λ_3, λ_4 are weights associated with the disc smoothness term (λ_1), cup data term (λ_2), cup smoothness term (λ_3) and the OD-OC interaction term (λ_4).

$(\lambda_1, \lambda_2, \lambda_3, \lambda_4)$	Train		Test	
	Dice	BLE	Dice	BLE
OD Segmentation				
A:(0, 0, 0, 0)	0.96/0.02	6.84/3.17	0.96/0.02	7.97/4.92
B:(1, 0, 0, 0)	0.97/0.02	6.41/3.37	0.97/0.02	6.64/3.55
C:(0, 0.1, 1, 0.1)	0.96/0.02	6.87/3.17	0.96/0.02	7.90/4.80
D:(1, 0.1, 1, 0.1)	0.97/0.02	6.42/3.36	0.97/0.02	6.61/3.55
Cup Segmentation				
E: (1, 0.1, 1, 0.1)	0.84/0.14	17.44/12.80	0.83/0.15	18.61/13.02
F:(1, 0.1, 1, 0)	0.77/0.23	24.64/25.52	0.70/0.27	32.32/30.27
G: (1, 0.1, 0, 0.1)	0.78/0.09	28.73/10.83	0.74/0.12	33.96/11.65
H: (1, 0, 1, 0.1)	0.82/0.14	20.13/13.87	0.82/0.17	21.49/16.25

smoothness and the disc-cup interaction terms with unit weight to the Disc unary term. Their optimal values were determined via a grid search over the Training set of DRISHTI-GS1. Tuning was done by searching values in $\{10^{-i} | -4 \leq i \leq 4, i \in Z\}$ and the parameters were finally set to $(\lambda_1 = 1, \lambda_2 = 0.1, \lambda_3 = 1, \lambda_4 = 0.1)$.

To analyze the impact of the various terms in Eq. (5) on OD and OC segmentation, we performed an additional set of experiments (Table 6) on the DRISHTI-GS1 test set by setting the weights of one or more of the energy terms to 0 while retaining the optimal weights for others. *OD segmentation* was analysed with parameter settings *A* through *D*. In setting *A*, the smoothness and pairwise terms are set to zero and the disc unary term alone is seen to be adequate for fairly accurate segmentation ($BLE = 7.97$ pixels on Test set). Addition of the disc smoothness term (setting *B*) marginally improves the BLE by 1.33 pixels on the Test set. The OD-cup interaction term has no significant impact (settings *C* and *D*) on OD segmentation.

OC segmentation was analysed in settings *E* through *H*. Inclusion of cup smoothness and OD-OC interaction terms are seen (Table 6) to significantly improve segmentation performance. The Dice value improves for these cases by 0.09 (*E* versus *G*) and 0.13 (*E* versus *F*), while BLE is nearly halved in both cases. The cup unary term (*E* versus *H*) only leads to a marginal improvement. The significant contribution from OD-OC interaction to OC segmentation indicates that the change in depth is more reliable in defining the OC boundary in comparison to the pallor edge information captured by the cup unary term. In contrast, the OD boundary is primarily defined by the color gradients captured by the disc unary term.

7. Conclusions

In this paper, we proposed a joint OD-OC segmentation framework that modeled depth based interaction between the OD and OC boundaries, using supervised depth estimates from the fundus image in addition to the color gradients at the OD and pallor boundaries. Despite training the supervised depth estimation method on just 30 fundus image-depth map pairs from the INSPIRE dataset, there was a good correlation between the estimated and true depth maps (mean ρ of 0.80).

The proposed joint segmentation method outperformed several state of the art methods including the existing joint OD-OC segmentation method in [61] for both OD and OC on multiple public datasets.

A comprehensive set of features derived from the OD-OC segmentation was able to distinguish between the Normal and glaucomatous images with an AUC of 0.85 on the RIM-ONE dataset. The experiments indicated that accurate segmentation in all sectors is critical for achieving good classification performance rather than the vertical direction alone.

Conflict of Interest Statement

The authors declare that there is no conflict of interest regarding the publication of this article.

Acknowledgment

This research was supported in part by the doctoral fellowship provided by Tata Consultancy Services (TCS) under their Research Scholarship Program.

References

[1] S. Resnikoff, D. Pascolini, D. Etya'ale, I. Kocur, R. Pararajasegaram, G.P. Pokharel, S.P. Mariotti, Global data on visual impairment in the year 2002, WHO Bull. 82 (11) (2004) 844–851.
[2] H.A. Quigley, A.T. Broman, The number of people with glaucoma worldwide in 2010 and 2020, Br.J.Ophthalmol. 90 (3) (2006) 262–267.
[3] L. Vijaya, R. George, P.G. Paul, M. Baskaran, H. Arvind, P. Raju, S.V. Ramesh, G. Kumaramanickavel, C. McCarty, Prevalence of open-angle glaucoma in a rural south indian population, Invest. Ophthalmol. Vis. Sci. 46 (12) (2005) 4461.
[4] S.Y. Shen, T.Y. Wong, P.J. Foster, J.-L. Loo, M. Rosman, S.-C. Loon, W.L. Wong, S.-M. Saw, T. Aung, The prevalence and types of glaucoma in malay people: the singapore malay eye study, Invest. Ophthalmol. Vis. Sci. 49 (9) (2008) 3846–3851.
[5] J.B. Jonas, G.C. Gusek, G. Naumann, Optic disc, cup and neuroretinal rim size, configuration and correlations in normal eyes., Invest. Ophthalmol. Vis. Sci. 29 (7) (1988) 1151–1158.
[6] M. Dinkin, M. Banks, J.F. Rizzo, Imaging the nerve fiber layer and optic disc, in: Pediatric Ophthalmol., Neuro-Ophthalmol., Genetics, 2008, pp. 99–118.
[7] P. Hrynchak, N. Hutchings, D. Jones, T. Simpson, A comparison of cup-to-disc ratio measurement in normal subjects using optical coherence tomography image analysis of the optic nerve head and stereo fundus biomicroscopy, Ophthalmic Physiol. Opt. 24 (6) (2004) 543–550.
[8] J. Xu, H. Ishikawa, G. Wollstein, R.A. Bilonick, K.R. Sung, L. Kagemann, K.A. Townsend, J.S. Schuman, Automated assessment of the optic nerve head on stereo disc photographs, Invest. Ophthalmol. Vis. Sci. 49 (6) (2008) 2512–2517.
[9] J. Xu, O. Chutatape, C. Zheng, P. Kuan, Three dimensional optic disc visualisation from stereo images via dual registration and ocular media optical correction, B.J.Ophthalmol. 90 (2) (2006) 181–185.
[10] A. Chakravarty, J. Sivaswamy, in: Medical Image Computing and Computer-Assisted Intervention MICCAI, 8673, 2014, pp. 747–754.
[11] S. Sekhar, W. Al-Nuaimy, A.K. Nandi, Automated localisation of retinal optic disk using hough transform, in: IEEE Int. Sym. on Biomedical Imaging. (ISBI), 2008, pp. 1577–1580.
[12] A. Bhuiyan, R. Kawasaki, T.Y. Wong, R. Kotagiri, A new and efficient method for automatic optic disc detection using geometrical features, in: World Congress on Medical Physics and Biomedical Engineering, Springer, 2009, pp. 1131–1134.
[13] A. Aquino, M.E. Gegúndez-Arias, D. Marín, Detecting the optic disc boundary in digital fundus images using morphological, edge detection, and feature extraction techniques, IEEE Trans. Med. Imaging 29 (11) (2010) 1860–1869.
[14] B. Dashtbozorg, A.M. Mendona, A. Campilho, Optic disc segmentation using the sliding band filter, Comput. Biol. Med. 56 (2015) 1–12.
[15] S. Roychowdhury, D.D. Koozekanani, S.N. Kuchinka, K.K. Parhi, Optic disc boundary and vessel origin segmentation of fundus images, IEEE J. Biomed. Health Inform. 20 (6) (2016) 1562–1574.
[16] D. Marin, M.E. Gegundez-Arias, A. Suero, J.M. Bravo, Obtaining optic disc center and pixel region by automatic thresholding methods on morphologically processed fundus images, Comput. Methods Programs Biomed. 118 (2) (2015) 173–185.
[17] M.P. Sarathi, M.K. Dutta, A. Singh, C.M. Travieso, Blood vessel inpainting based technique for efficient localization and segmentation of optic disc in digital fundus images, Biomed. Signal Process Control 25 (2016) 108–117.
[18] J. Lowell, A. Hunter, D. Steel, A. Basu, R. Ryder, E. Fletcher, L. Kennedy, Optic nerve head segmentation, IEEE Trans. Med. Imaging 23 (2) (2004) 256–264.
[19] D. Wong, J. Liu, J. Lim, X. Jia, F. Yin, H. Li, T. Wong, Level-set based automatic cup-to-disc ratio determination using retinal fundus images in argali, in: IEEE International Conference Engineering in Medicine and Biology Society, 2008, pp. 2266–2269.
[20] G.D. Joshi, J. Sivaswamy, S. Krishnadas, Optic disk and cup segmentation from monocular color retinal images for glaucoma assessment, IEEE Trans. Med. Imaging 30 (2011) 1192–1205.
[21] J.R.H. Kumar, A.K. Pediredla, C.S. Seelamantula, Active discs for automated optic disc segmentation, in: 2015 IEEE Global Conference on Signal and Information Processing (GlobalSIP), 2015, pp. 225–229.
[22] B. Harangi, R.J. Qureshi, A. Csutak, T. Peto, A. Hajdu, Automatic detection of the optic disc using majority voting in a collection of optic disc detectors, in: IEEE International Symposium on Biomedical Imaging, 2010, pp. 1329–1332.
[23] H. Li, O. Chutatape, Boundary detection of optic disk by a modified asm method, Pattern Recognit. 36 (9) (2003) 2093–2104.

[24] F. Yin, J. Liu, S.H. Ong, Y. Sun, D.W. Wong, N.M. Tan, C. Cheung, M. Baskaran, T. Aung, T.Y. Wong, Model-based optic nerve head segmentation on retinal fundus images, in: IEEE International Conference Engineering in Medicine and Biology Society, 2011, pp. 2626–2629.
[25] M.D. Abramoff, W.L. Alward, E.C. Greenlee, L. Shuba, C.Y. Kim, J.H. Fingert, Y.H. Kwon, Automated segmentation of the optic nerve head from stereo color photographs using physiologically plausible feature detectors, Invest. Ophthalmol. Vis. Sci. 48 (2007) 1665.
[26] J. Cheng, J. Liu, Y. Xu, F. Yin, D.W.K. Wong, N.-M. Tan, D. Tao, C.-Y. Cheng, T. Aung, T.Y. Wong, Superpixel classification based optic disc and optic cup segmentation for glaucoma screening, IEEE Trans. Med. Imaging 32 (6) (2013) 1019–1032.
[27] P.L. Rosin, D. Marshall, J.E. Morgan, Multimodal retinal imaging: new strategies for the detection of glaucoma, in: International Conference of Image Processing, 3, 2002, pp. III–137.
[28] M.-L. Huang, H.-Y. Chen, J.-J. Huang, Glaucoma detection using adaptive neuro-fuzzy inference system, Expert Syst. Appl. 32 (2) (2007) 458–468.
[29] J. Xu, O. Chutatape, E. Sung, C. Zheng, P.C.T. Kuan, Optic disk feature extraction via modified deformable model technique for glaucoma analysis, Pattern Recognit. 40 (2007) 2063–2076.
[30] T. Nakagawa, Y. Hayashi, Y. Hatanaka, A. Aoyama, T. Hara, A. Fujita, M. Kakogawa, H. Fujita, T. Yamamoto, Three-dimensional reconstruction of optic nerve head from stereo fundus images and its quantitative estimation, in: IEEE International Conference Engineering in Medicine and Biology Society, 2007, pp. 6747–6750.
[31] M.S. Miri, M.D. Abràmoff, K. Lee, M. Niemeijer, J.K. Wang, Y.H. Kwon, M.K. Garvin, Multimodal segmentation of optic disc and cup from sd-oct and color fundus photographs using a machine-learning graph-based approach, IEEE Trans. Med. Imaging 34 (9) (2015) 1854–1866.
[32] G.D. Joshi, J. Sivaswamy, K. Karan, S. Krishnadas, Optic disk and cup boundary detection using regional information, in: IEEE International Symposium on Biomedical Imaging. (ISBI), 2010, pp. 948–951.
[33] S. Bhartiya, R. Gadia, H.S. Sethi, A. Panda, Clinical evaluation of optic nerve head in glaucoma, J. Current Glaucoma Pract. 4 (3) (2010) 115–132.
[34] W.W.K. Damon, J. Liu, T.N. Meng, Y. Fengshou, W.T. Yin, Automatic detection of the optic cup using vessel kinking in digital retinal fundus images, in: IEEE International Symposium on Biomedical Imaging. (ISBI), 2012, pp. 1647–1650.
[35] Y. Hatanaka, Y. Nagahata, C. Muramatsu, S. Okumura, K. Ogohara, A. Sawada, K. Ishida, T. Yamamoto, H. Fujita, Improved automated optic cup segmentation based on detection of blood vessel bends in retinal fundus images, in: International Conference of the IEEE Engineering in Medicine and Biology Society, 2014, pp. 126–129.
[36] J.G. Zilly, J.M. Buhmann, D. Mahapatra, Boosting convolutional filters with entropy sampling for optic cup and disc image segmentation from fundus images, in: International Workshop on Machine Learning in Medical Imaging, Springer, 2015, pp. 136–143.
[37] S. Sedai, P.K. Roy, D. Mahapatra, R. Garnavi, Segmentation of optic disc and optic cup in retinal fundus images using shape regression, in: 2016 38th Annual International Conference of the IEEE Engineering in Medicine and Biology Society (EMBC), 2016, pp. 3260–3264.
[38] L. Tang, M.K. Garvin, K. Lee, W.L. Alward, Y.H. Kwon, M.D. Abramoff, Robust multiscale stereo matching from fundus images with radiometric differences, IEEE Trans. Pattern Anal. Mach. Intell. 33 (2011) 2245–2258.
[39] J. Sivaswamy, S. Krishnadas, A. Chakravarty, G.D. Joshi, Ujjwal, T.A. Syed, A comprehensive retinal image dataset for the assessment of glaucoma from the optic nerve head analysis, JSM Biomed. Imaging Data Papers 2 (2015) 1004.
[40] F. Fumero, S. Alayón, J. Sanchez, J. Sigut, M. Gonzalez-Hernandez, Rim-one: An open retinal image database for optic nerve evaluation, in: Computer-Based Medical Systems (CBMS), International Symposium on, 2011, pp. 1–6.
[41] E.J. Carmona, M. Rincón, J. García-Feijoó, J.M. Martínez-de-la Casa, Identification of the optic nerve head with genetic algorithms, Artif. Intell. Med. 43 (3) (2008) 243–259.
[42] E. Decencire, X. Zhang, G. Cazuguel, B. Lay, B. Cochener, C. Trone, P. Gain, R. Ordonez, P. Massin, A. Erginay, B. Charton, J.-C. Klein, Feedback on a publicly distributed image database: the messidor database, Image Anal. Stereol. 33 (3) (2014) 231–234.
[43] Expert system for early automatic detection of diabetic retinopathy by analysis of digital retinal images: http://uhu.es/retinopathy/eng/bd.php, 2012.
[44] A. Giachetti, L. Ballerini, E. Trucco, Accurate and reliable segmentation of the optic disc in digital fundus images, J. Med. Imaging 1 (2) (2014) 024001.
[45] H. Yu, E.S. Barriga, C. Agurto, S. Echegaray, M.S. Pattichis, W. Bauman, P. Soliz, Fast localization and segmentation of optic disk in retinal images using directional matched filtering and level sets, IEEE Trans. IT Biomed. 16 (4) (2012) 644–657.
[46] S. Morales, V. Naranjo, J. Angulo, M. Alcañiz, Automatic detection of optic disc based on PCA and mathematical morphology, IEEE Trans. Med. Imaging 32 (4) (2013) 786–796.
[47] M. Bertalmio, G. Sapiro, V. Caselles, C. Ballester, Image inpainting, in: Proceedings of the 27th Annual Conference on Computer Graphics and Interactive Techniques, 2000, pp. 417–424.
[48] B.V. Funt, M.S. Drew, M. Brockington, Recovering shading from color images, in: ECCV, 1991, pp. 124–132.
[49] P. sing Tsai, M. Shah, Shape from shading using linear approximation, Image Vis. Comput. 12 (1994) 487–498.
[50] S.Y. Elhabian, Hands on Shape from Shading, Technical Report, 2008. Technical Report, May 2008.
[51] H. Akaike, A new look at the statistical model identification, IEEE Trans. Automat. Control 19 (6) (1974) 716–723.
[52] J. Malik, S. Belongie, J. Shi, T. Leung, Textons, contours and regions: cue integration in image segmentation, In International Conference on Computer Vison (ICCV), 1999.
[53] D.R. Hardoon, S. Szedmak, J. Shawe-Taylor, Canonical correlation analysis: an overview with application to learning methods, Neural Comput. 16 (12) (2004) 2639–2664.
[54] J. Yang, Z. Wang, Z. Lin, S. Cohen, T. Huang, Coupled dictionary training for image super-resolution, IEEE Trans. Image Process. 21 (8) (2012) 3467–3478.
[55] S. Yu, W. Ou, X. You, Y. Mou, X. Jiang, Y. Tang, Single image rain streaks removal based on self-learning and structured sparse representation, in: 2015 IEEE China Summit and International Conference on Signal and Information Processing (ChinaSIP), 2015, pp. 215–219.
[56] W. Ou, X. You, D. Tao, P. Zhang, Y. Tang, Z. Zhu, Robust face recognition via occlusion dictionary learning, Pattern Recognit. 47 (4) (2014) 1559–1572.
[57] Z. He, S. Yi, Y.M. Cheung, X. You, Y.Y. Tang, Robust object tracking via key patch sparse representation, IEEE Trans. Cybern. 47 (2) (2017) 354–364.
[58] M. Aharon, M. Elad, A. Bruckstein, k -svd: an algorithm for designing overcomplete dictionaries for sparse representation, Signal Process. IEEE Trans. 54 (11) (2006) 4311–4322.
[59] V. Kolmogorov, Convergent tree-reweighted message passing for energy minimization, IEEE Trans. Pattern Anal. Mach. Intell. 28 (10) (2006) 1568–1583.
[60] G.D. Joshi, J. Sivaswamy, S. Krishnadas, Depth discontinuity-based cup segmentation from multiview color retinal images, IEEE Trans. IT Biomed. 59 (6) (2012) 1523–1531.
[61] Y. Zheng, D. Stambolian, J. OBrien, J.C. Gee, Optic disc and cup segmentation from color fundus photograph using graph cut with priors, in: Medical Image Computing and Computer-Assisted Intervention MICCAI, 2013, pp. 75–82.
[62] S. Morales, V. Naranjo, D. Perez, A. Navea, M. Alcaniz, Automatic detection of optic disc based on PCA and stochastic watershed, in: European Signal Processing Conference (EUSIPCO), 2012, pp. 2605–2609.
[63] T. Walter, J.-C. Klein, P. Massin, A. Erginay, A contribution of image processing to the diagnosis of diabetic retinopathy-detection of exudates in color fundus images of the human retina, IEEE Trans. Med. Imaging 21 (10) (2002) 1236–1243.